

Trapped motion around the Pribilof Islands in the Bering Sea

Zygmunt Kowalik

Institute of Marine Science, University of Alaska, Fairbanks

Phyllis Stabeno

Pacific Marine Environmental Laboratory, NOAA, Seattle, Washington

Abstract. Observations in the region of the Pribilof Islands and Canyon (PIC) reveal a clockwise circulation around the group of islands and around each of the two largest islands, St. Paul and St. George. Six current meters deployed around St. Paul Island revealed a steady clockwise flow around the island, which was strongest south of the island and weakest to the east. We use a high-resolution tidal model in the PIC region to show that this flow pattern results from tidal rectification over the shallow topography tides. Tidal residual currents of 10–15 cm s⁻¹ were predicted by the model, compared to mean currents of 5–20 cm s⁻¹ observed at the mooring sites. Both diurnal and semidiurnal tidal oscillations contribute to the clockwise circulation around the islands. In the diurnal band the enhanced currents occur also at the shelf slope where a tidal wave generates a shelf wave due to resonance with topography. In the PIC region the main shelf wave occurs in the Pribilof Canyon where both observations and measurements show enhancement of the diurnal tidal currents.

1. Introduction

The eastern half of the Bering Sea consists of a broad (>500 km), flat continental shelf that is interrupted by only a few island groups. The southernmost of these, the Pribilof Islands, are located near the shelf break and separated from Pribilof Canyon by only 30 km (Figure 1). On the southeast Bering Sea shelf there is a persistent, although weak (5 cm s⁻¹) flow toward the northwest along the 100 m isobath [Reed and Stabeno, 1996], which when confined by the narrow shelf south of the Pribilof Islands accelerates to 20 cm s⁻¹. The flow turns northward west of St. George Island; north of St. Paul Island the flow bifurcates with most continuing northward along the 100 m isobath, but a portion flowing weakly eastward (Figure 1). The mean currents provide nutrients to this rich ecosystem and transport planktonic material into the region. Although the low-frequency flow around the islands is persistent, the kinetic energy in the vicinity of the Pribilof Islands is dominated (>90%) by tidal motion [Pearson *et*

al., 1981; Schumacher and Stabeno, 1998; Coachman, 1986]. Because of the locations of these islands near the shelf break, large populations of marine mammals, seabirds and fish can be found here. Surrounding the two largest islands is a well-mixed region that is stirred by tidal currents. Circulation around the islands could trap foreign material near the islands affecting the productivity of these waters. Understanding the flow patterns around these islands is necessary to being able to protect this rich ecosystem.

The interaction of tides and currents with bottom topography around islands, seamounts, and canyons often leads to current enhancement, and as a consequence, the nonlinear interactions become stronger in such regions [Haidvogel *et al.*, 1993; Brink, 1995; Kowalik, 1999]. Seamounts and islands depict symmetry while interacting with various flows; the flow interacting with canyons leads to an asymmetrical pattern which depends on the direction of the alongshore flow [Klinck, 1996]. In the case of a tidal current this asymmetry may generate upwelling on one side of a canyon and downwelling on the other side. Enhanced tidal currents, through advective terms and bottom friction lead to stronger nonlinear interactions resulting in the new periodical oscillations and residual circulation. Observations and model computations of the oscillatory tidal flow interact-

Copyright 1999 by the American Geophysical Union.

Paper number 1999JC900209.
0148-0227/99/1999JC900209\$09.00

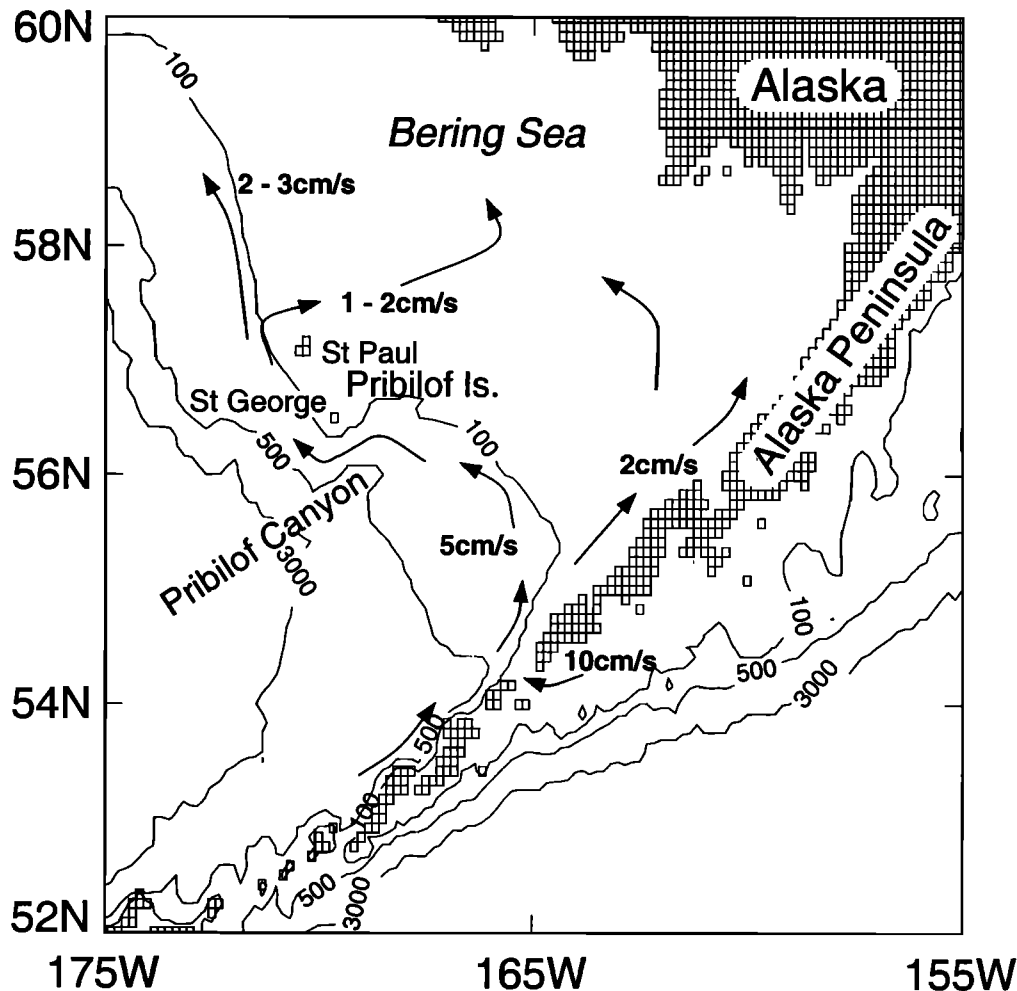


Figure 1. An area map and schematic of the mean circulations in the eastern Bering Sea based on *Schumacher and Stabeno* [1998].

ing with bottom topography demonstrate well-developed rectilinear motion around banks and islands [Zimmerman, 1978; Loder, 1980]. *Pingree and Maddock* [1985] showed how advection and stretching of the oscillating vorticity by the oscillating currents around the islands is rectified into residual circular motion. The tidal wave around an island is a superposition of two waves, a primary wave that propagates over the large scale and a secondary wave trapped around an island [Kowalik and Proshutinsky, 1995]. While the primary wave changes sea level in the entire domain, the trapped wave propagates clockwise around the island with the same period. The interaction of wind-driven motion with nonuniform bathymetric features can result in persistent trapped flow around seamounts and in submarine canyons. *Gjevik and Moe* [1994] investigated time-dependent wind-forced trapped motion at the bank in the Norwegian Sea for both

barotropic and baroclinic motion and delineated a circular flow around the bank.

Residual tidal currents trapped in proximity to the bathymetric features can be an important mechanism contributing to the mean circulation in the Bering Sea. *Mofjeld et al.* [1984] presented estimates of residual currents by fitting simple tidal waves to the observed tidal currents from two stations at the Bering Sea shelf. Estimated residual currents were smaller than 1 cm s^{-1} . *Schumacher and Kinder* [1983] arrived at a similar residual velocity over the open Bering Sea shelf. *Liu and Leendertse* [1990] demonstrated, through the various shelf models, the importance of residual currents in the Bering Sea circulation. In their model a resolution of about 20 km was used to investigate residual tidal currents of both barotropic and baroclinic origin. Close to the Bering Sea slope the model depicted residual currents from 2 to 5 cm s^{-1} .

In this paper we present results of observations from both moored instruments and from satellite-tracked drifters which reveal circular flow around the island group. We, then, use a numerical model to interpret and identify mechanisms which result in this trapped motion around the Pribilof Islands.

2. Satellite-Tracked Drifters

Satellite-tracked drifters have been deployed on the Bering Sea shelf for 10 years as part of Fisheries Oceanography Coordinated Investigations (FOCI). We show the trajectories from three drifters. The drifter deployed in 1993 had a Tristar drogue, while the two buoys from 1995 had WOCE-type drogues. All drifting buoys were drogued at 40 m and thus were below the mixed layer. Each buoy had a tilt switch that indicated when a drogue was lost, and only data from buoys that retained drogues are presented here. Position fixes were received from Service Argos and obviously erroneous positions were deleted. Approximately 12 fixes were obtained per day, with a standard position error of 0.18 km [Reed and Stabeno, 1996].

Typically, drifters deployed on the outer shelf (water depth 100 m to 180 m) and the slope are advected northwestward to the vicinity of the Pribilof Islands. The two drifters shown here (Figure 2) were deployed in May 1995 followed this pattern. They were transported northward along the 100 m isobath at 3–4 cm s⁻¹. Velocities more than doubled over the narrow portion of the shelf south of St. George Island. West of the Pribilof Islands, the velocities were 10–12 cm s⁻¹ and much weaker (4–6 cm s⁻¹) east of the islands. After reaching the Pribilof Islands, the buoys were entrained into the flow around the islands. One drifter circled St. Paul and then continued northward. The second drifter circled both islands and then reentered the Bering Slope Current. Tidal loops are clearly evident in the trajectories.

In 1993 a satellite-tracked buoy was deployed on the Bering Sea shelf south of the Pribilof Islands. It was transported northwestward to the vicinity of St. George Island where it circled the island 7 times in 60 days before it lost its drogue. One period of consistent clockwise circulation is shown in Figure 3. Mean circular velocity was about 20 cm s⁻¹, and mean speeds did not appear to differ markedly on the different sides of the island. Diurnal tidal ellipses are evident, although very small. The buoy trajectories in a water depth of less than 40 m can be deflected from following the actual water mo-

tion due to the dragging of the drogue on the seabed. Through this interaction with the bottom, the buoy can rectify tidal flow. Future investigations ought to clarify how important this bottom interaction is for the estimated drift of a buoy in the island proximity.

3. Equations and Boundary Conditions for the Tidal Model

To obtain high-resolution tides around St. Paul Island, we start from the large-scale model of the entire Bering Sea with a resolution of 5' along latitude and 10' along longitude (Figure 4). At the latitude of 60°N both steps are equal to 9.26 km; therefore we shall use this distance to describe the large-scale numerical lattice. For the entire Bering Sea a spherical system of coordinates is used. The results of computations from this domain serve to construct the boundary conditions for the domain around Pribilof Islands (Figure 4). A rectangular system of coordinates is used for the Pribilof Islands with a resolution of 1.852 km. The results of computations from the latter domain are applied to establish boundary conditions for the computations around St. Paul with a resolution of 617 m. For computations of tide amplitudes and phases we shall use the vertically integrated equations of motion and continuity. Here these equations are given in the spherical coordinate system [Gill, 1982]:

$$\frac{\partial u}{\partial t} + \frac{u}{R \cos \phi} \frac{\partial u}{\partial \lambda} + \frac{v}{R} \frac{\partial u}{\partial \phi} - fv - \frac{uv \sin \phi}{R \cos \phi} = -\frac{g}{R \cos \phi} \frac{\partial}{\partial \lambda} (\alpha \zeta - \beta \zeta_0) - \frac{\tau_\lambda^b}{\rho H} + Au, \quad (1)$$

$$\frac{\partial v}{\partial t} + \frac{u}{R \cos \phi} \frac{\partial v}{\partial \lambda} + \frac{v}{R} \frac{\partial v}{\partial \phi} + fv + \frac{uv \sin \phi}{R \cos \phi} = -\frac{g}{R} \frac{\partial}{\partial \phi} (\alpha \zeta - \beta \zeta_0) - \frac{\tau_\phi^b}{\rho H} + Av, \quad (2)$$

$$\frac{\partial \zeta}{\partial t} + \frac{1}{R \cos \phi} \frac{\partial (Hu)}{\partial \lambda} + \frac{1}{R \cos \phi} \frac{\partial (Hv \cos \phi)}{\partial \phi} = 0. \quad (3)$$

The operator (A) in the horizontal friction term in (1) and (2) is

$$A = N_h \left(\frac{1}{R^2 \cos^2 \phi} \frac{\partial^2}{\partial \lambda^2} + \frac{1}{R^2 \cos \phi} \frac{\partial}{\partial \phi} \left(\cos \phi \frac{\partial}{\partial \phi} \right) \right). \quad (4)$$

The bottom friction components are taken as

$$\tau_\lambda^b = \rho r u \sqrt{u^2 + v^2}; \quad \tau_\phi^b = \rho r v \sqrt{u^2 + v^2}. \quad (5)$$

In (5), r denotes the bottom drag coefficient which will be taken as $r = 2.9 \times 10^{-3}$.

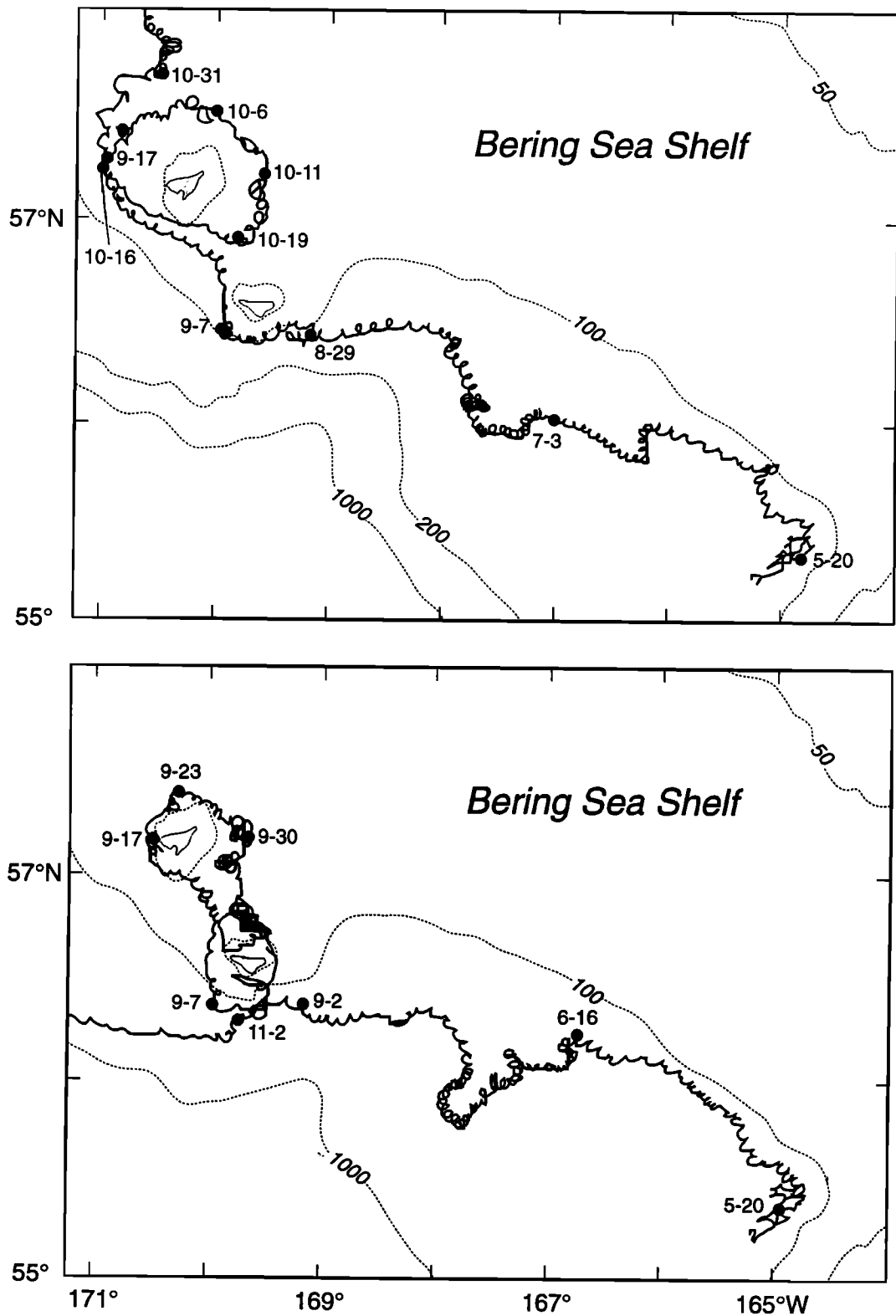


Figure 2. Trajectories of two satellite-tracked drifting buoys deployed on May 18, 1995. Both buoys were transported northwestward along the 100 m isobath. Tidal loops are evident in both trajectories. Mean velocity along the 100 m isobath was 3–4 cm s^{-1} . Both buoys accelerated south of St. George to 6–10 cm s^{-1} . The northward velocity of the westside of the Pribilof Islands for both buoys was 10–12 cm s^{-1} . (top) Buoy A circled St. Paul in 30 days at an average velocity of 8 cm s^{-1} . (bottom) Buoy B had a southward average velocity of 4–5 cm s^{-1} on the east side of the Pribilof Islands.

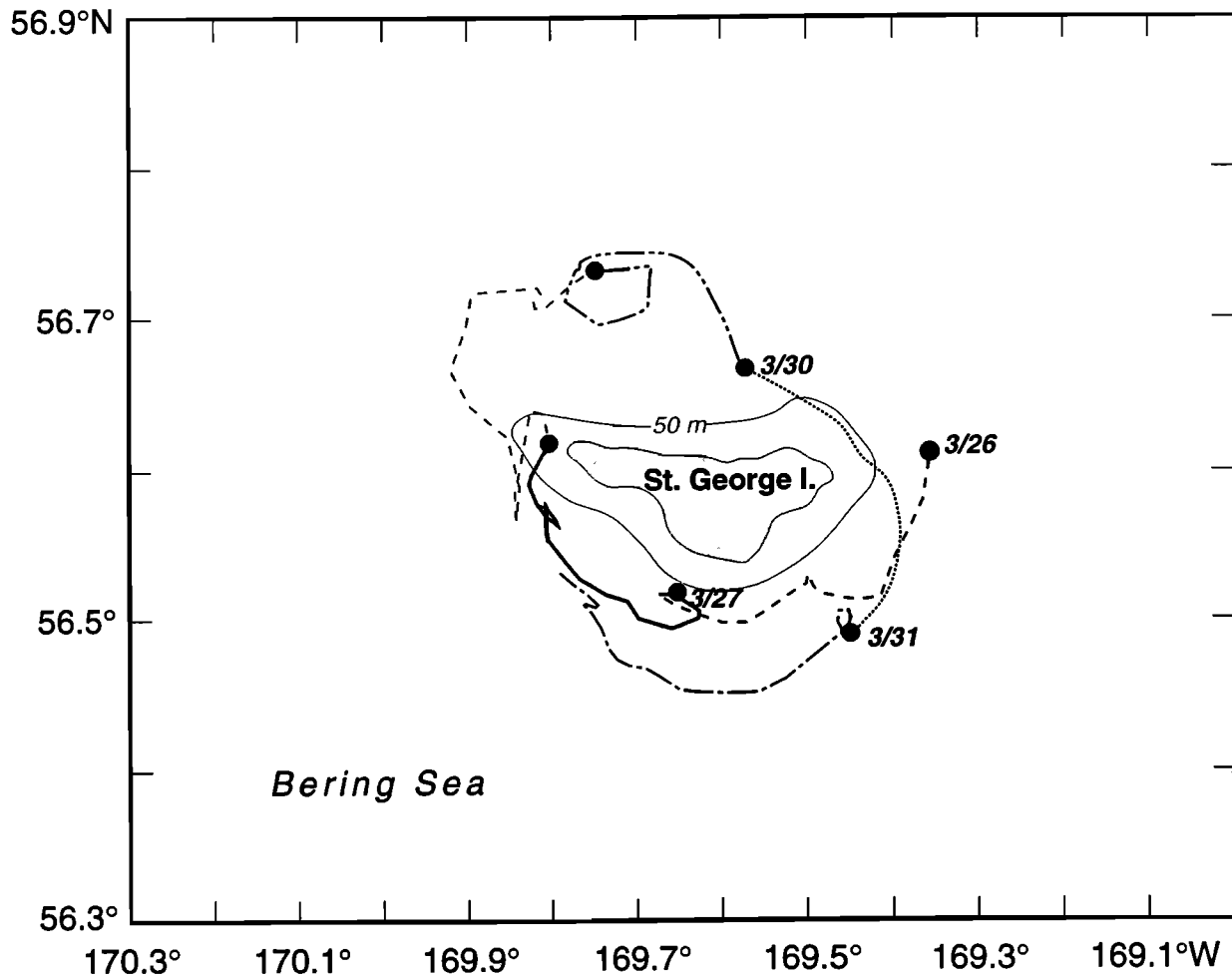


Figure 3. Trajectory of a satellite-tracked drifting buoy that was deployed on March 8, 1993, on the southeastern Bering Sea shelf. Six days of the trajectory are shown, during which the buoy circles the island about 1.3 times. Mean velocity around the island was 20 cm s^{-1} .

The following notations have been used in the above equations: λ , ϕ denote longitude and latitude; t is time; ζ is free surface elevation; u and v are velocity components along longitude and latitude, respectively; ρ is water density; N_h is horizontal eddy viscosity; H denotes depth (it does not include sea level); f is Coriolis parameter; g denotes gravity acceleration; R is radius of the Earth; ζ_0 denotes the equilibrium tide; α and β are parameters accounting for tidal potential perturbations.

The tidal forcing is described in (1) and (2) through the terms which are multiplied by coefficients α and β . These terms include the tide-generating potential, but they also contain various corrections due to Earth tide and ocean loading. Coefficient α defines ocean loading; its value ranges from 0.940 to 0.953. The term $\beta\zeta_0$ includes both the tide-generating potential and

the correction due to the Earth tide. It is usually expressed as [Hendershott, 1977]

$$\beta\zeta_0 = (1 + k - h)\zeta_0. \quad (6)$$

Here k and h denote Love numbers, which are equal to 0.302 and 0.602, respectively. These numbers are averaged over all tidal constituents.

In the ensuing computations one additional simplification is introduced. The influence of the sea ice on the tide is neglected. The Bering Sea is only partly covered by sea ice. The influence of the pack ice on tides is usually quite small and can be neglected. The influence of the shore fast ice is usually strong and ought to be taken into account. Data described by Mofjeld [1986] from the northwestern shelf show that the tidal harmonic constants change seasonally, probably due to the pack ice. The di-

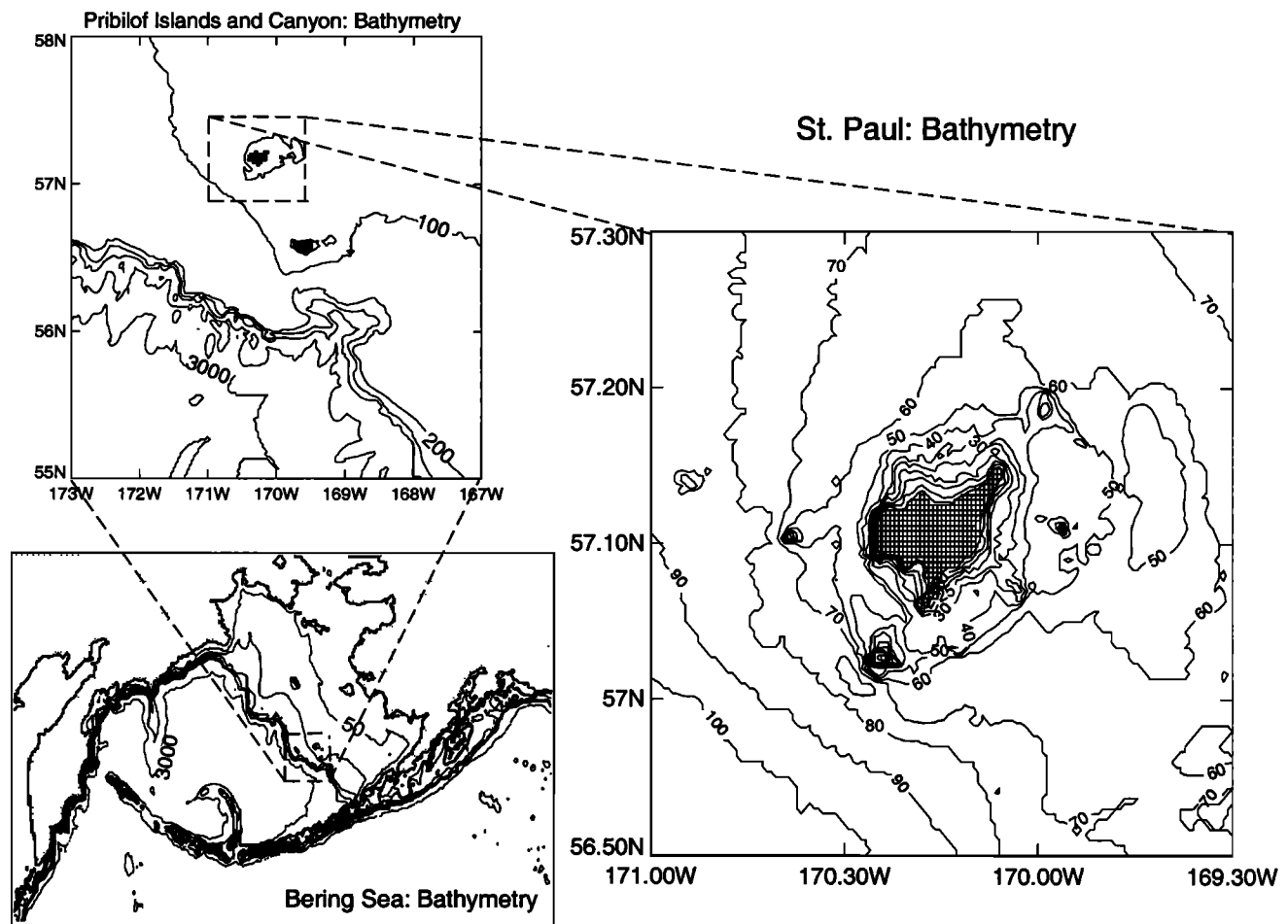


Figure 4. Computational domains and bottom topography: Bering Sea, grid resolution 9.26 km; Pribilof Islands and Canyon, grid resolution 1.852 km; St. Paul Island, grid resolution 617 m.

urnal amplitude increased and semidiurnal amplitude decreased during winter. The increase and decrease amounted to a few percent of the mean values. The relatively high changes in amplitude (40% of the mean amplitude) occurred close to the shoreline under the shore fast ice in the Norton Sound, Bering Sea [Johnson and Kowalik, 1986]. Sea ice, on average, is in the vicinity of Pribilof Island about 3 weeks a year, and fast ice is never generated in this region.

Initially, the dependent variables in the integration domain are taken as zero:

$$\zeta(\lambda, \phi)_{t=0} = 0, \quad (7)$$

$$u(\lambda, \phi)_{t=0} = 0, \quad v(\lambda, \phi)_{t=0} = 0. \quad (8)$$

Along the solid boundary S we assume a no-slip condition for water transport:

$$u_S(\lambda, \phi, t) = 0, \quad v_S(\lambda, \phi, t) = 0. \quad (9)$$

The model is forced through the open boundary O of the domain, and on this boundary the sea level is given as

$$\zeta_o = \zeta(\lambda, \phi, t). \quad (10)$$

In the entire Bering Sea (Figure 4) along the open boundaries, amplitudes and phases for every tidal constituent are specified. This is accomplished through the results obtained from surface and satellite observations and large-scale numerical models [Kowalik, 1999].

Embedding of the regional (finer resolution) subdomains within the domains with coarser resolution requires coupling of these regions along the common boundary. The sea level calculated in the coarser-grid domain is employed to prescribe elevations on the open boundaries of the finer-resolution domain. The coarser grid is connected to the finer grid through linear interpolation, and the variables from the coarser

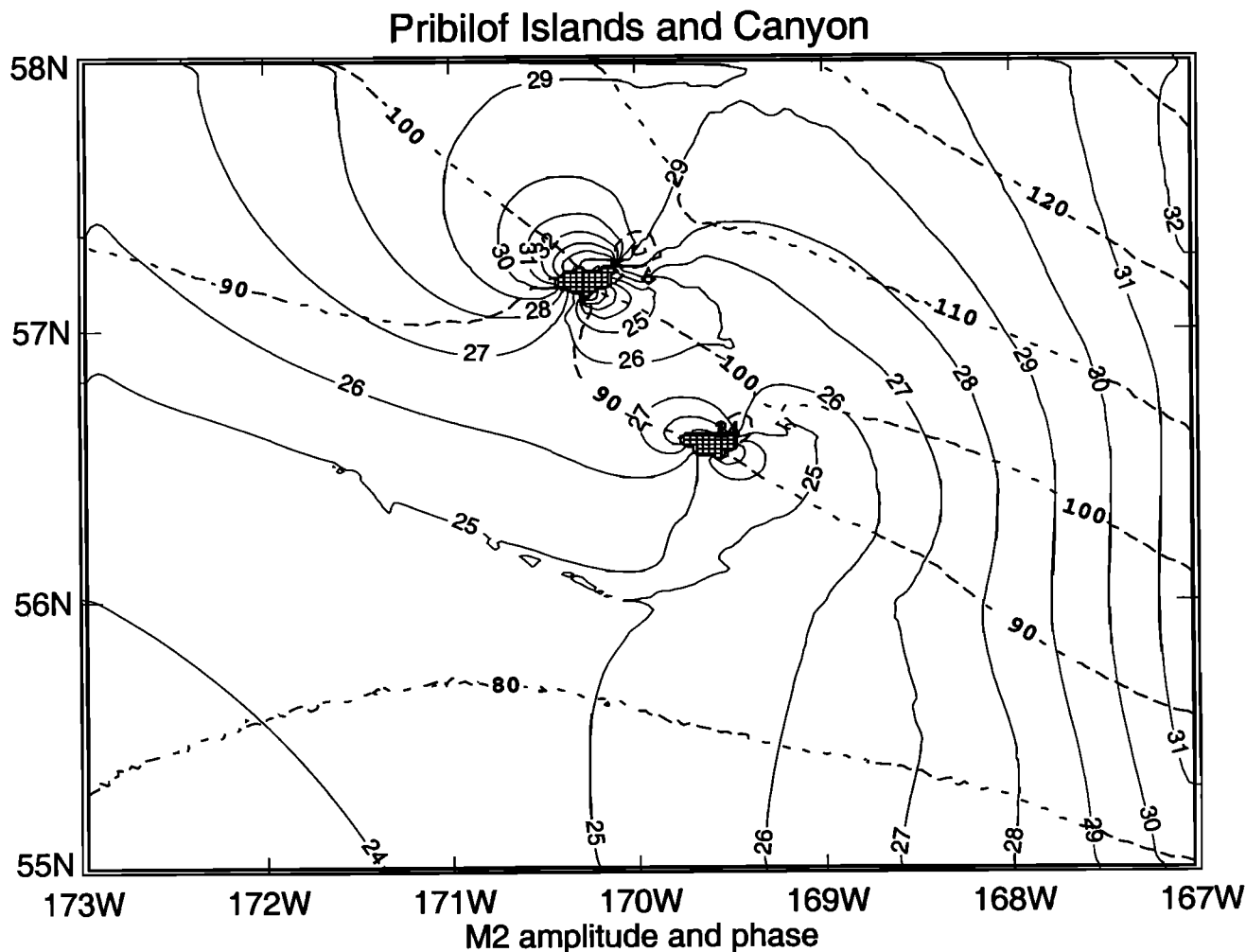


Figure 5. Calculated amplitude (solid lines, in centimeters) and phase (dashed lines, in degrees) of surface elevation for the semidiurnal M_2 tide in the Pribilof Island and Canyon domain.

grid are used directly as a boundary condition for the finer grid only. There is no two-way dynamical coupling.

In the calculation process, along with the refining of numerical grid, it is necessary to take into account dependence of the horizontal exchange of momentum on the scale of numerical grid. The computations were carried out with $N_h = 2.0 \times 10^7$, $N_h = 5 \times 10^6$, and $N_h = 5 \times 10^5$ cm^2s^{-1} for the space grid of 9.26 km, 1.852 km, and 617 m, respectively.

4. Tides in the Pribilof Islands and Canyon

To understand the origin of the trapped circulation around Pribilof Islands which was revealed by satellite-tracked drifters, we investigate tide dynamics around these islands. Four major tidal constituents are considered, i.e., M_2 ,

N_2 , K_1 , and O_1 . The results from the Bering Sea model serve as a boundary condition for the fine-scale model in the Pribilof Islands and Canyon (PIC) domain (Figure 4). In this domain a resolution of 1852 m is used. Harmonic constants for the major tidal constituents and residual tidal currents are obtained by analyzing a 29 day series of computed tidal elevations and tidal currents.

A tide wave enters the Bering Sea as a progressive wave from the North Pacific Ocean through Aleutian Island passages [Pearson *et al.*, 1981]. The PIC domain is located over both the Bering Sea shelf and the slope. In this region the tides propagate from the basin into a shallow domain and are enhanced in both amplitude and velocity. To identify differences in semidiurnal and diurnal tidal waves, results of calculations for the M_2 and K_1 waves are considered. In Figure 5, amplitude and phase of

surface elevation for the M_2 tide are given. Sea level amplitude slowly changes from 24 cm over the slope to 31 cm over the shelf. An interesting pattern in the sea level occurs around Pribilof Islands. The sea level depicts a dipole structure with the minimum located at the southeastern shores and the maximum at northern shores. Especially conspicuous is a 15 cm sea level change around St. Paul Island. This distribution of the sea level agrees well with the general pattern of interaction of tide wave and an island constructed by Proudman [Defant, 1960, p. 358]. Figure 6 depicts the maximum of M_2 tidal currents. The sluggish flow over the basin of the order of 1 cm s^{-1} is enhanced over shelf break to $5\text{--}10 \text{ cm s}^{-1}$. The isolines of the current magnitudes tend to follow bathymetry contours. This is clear in Pribilof Canyon where complex bathymetry occurs. Around Pribilof Islands due to topographic amplification and non-linear interactions in the shallow water, velocities as large as 50 cm s^{-1} are generated.

The tidal dynamics in the diurnal band of oscillations is illustrated through the major K_1 constituent. Figure 7 depicts a general pattern of slowly varying sea level from southwest to northeast, with the maximum of amplitude, ($>39 \text{ cm}$), occurring along the shelf slope. A number of local sea level maxima can be discerned not only near the islands but also along the shelf slope close to the 200 m depth contour. Especially pronounced is the maximum at southeastern flank of Pribilof Canyon. The K_1 maximum currents are given in Figure 8. Although in the large-scale pattern one can see the enhancement of current from deep basin to the shelf, the total picture is more complex than observed in M_2 tide. The enhancement of currents around the islands is not the sole feature. Along the shelf slope, especially in the region of Pribilof Canyon, the local enhancement is also apparent. At the midslope location in Pribilof Canyon (272 m depth), long-term current meter records analyzed by Schumacher and

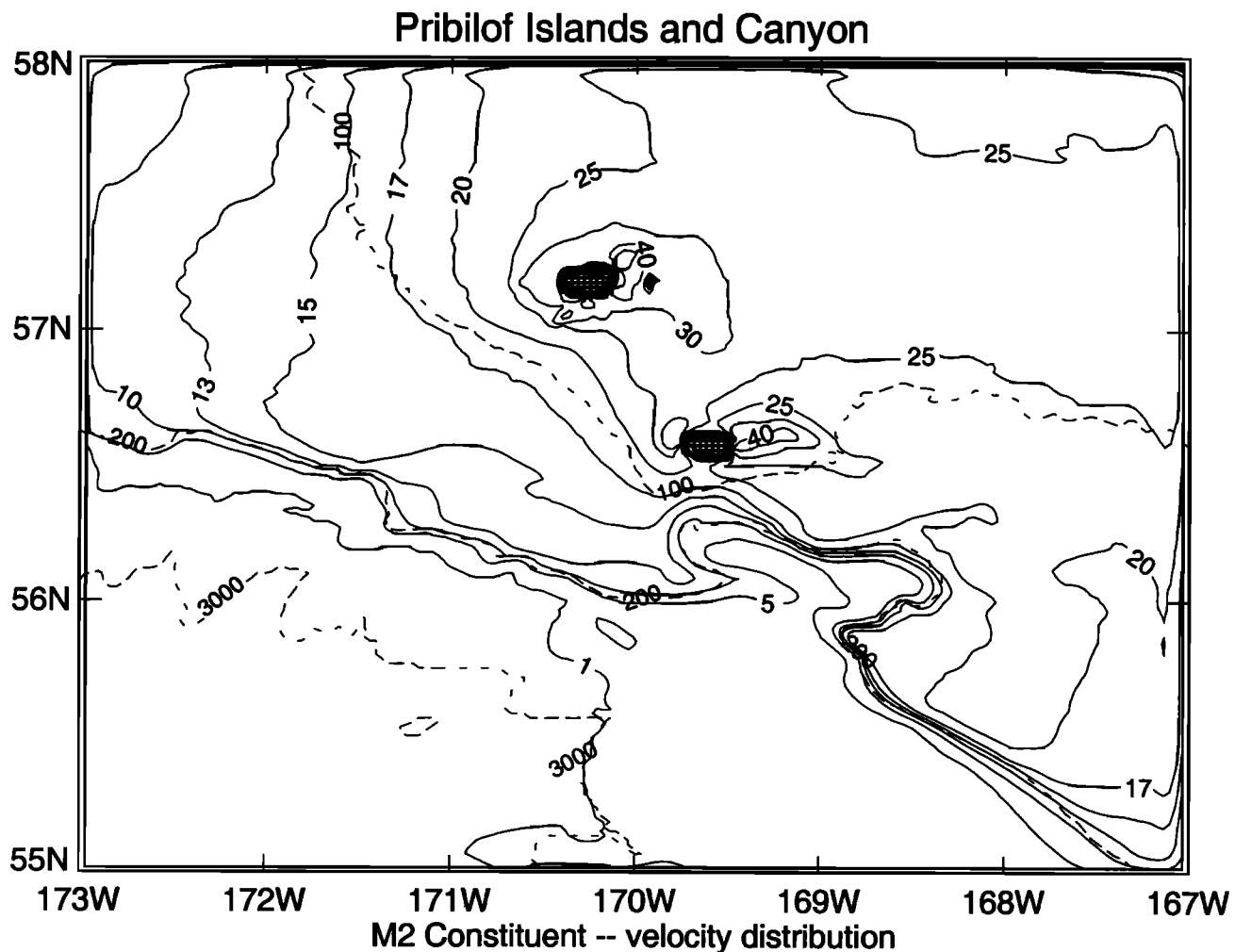


Figure 6. Contours of the maximum tidal currents (cm s^{-1}) of the M_2 wave in the Pribilof Island and Canyon domain. Dashed lines denote depth in meters.

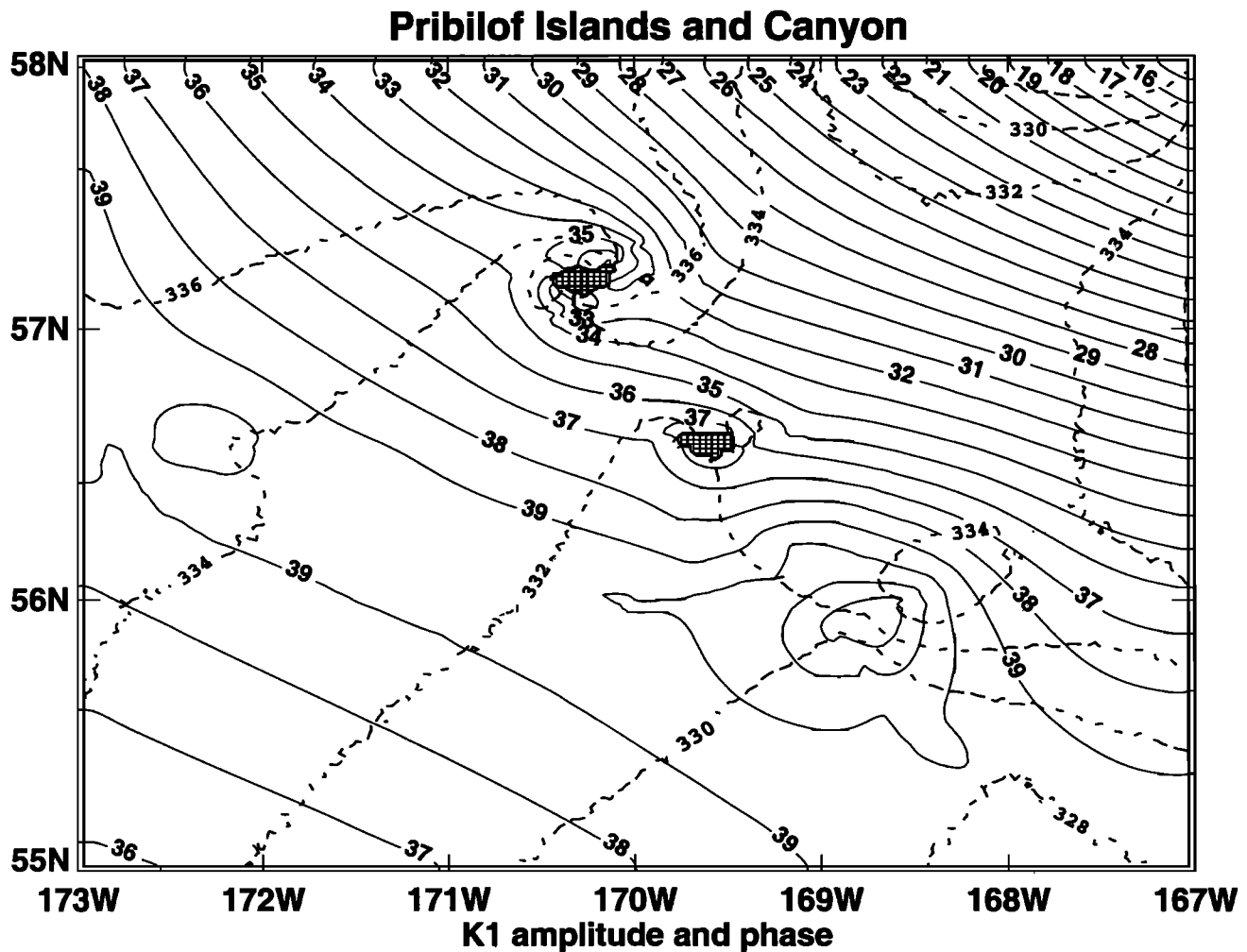


Figure 7. Calculated amplitude (solid lines, in centimeters) and phase (dashed lines, in degrees) of surface elevation for the diurnal K_1 tide in the Pribilof Island and Canyon domain.

Reed [1992] corroborate this local enhancement of the diurnal currents. The local regions of enhanced diurnal currents are related to the sea level changes observed in Figure 7. The important conclusion is that the diurnal tide can generate enhanced currents not only in the shallow domains around islands but also in the deeper domains in the shelf slope region as well.

5. Tides Around St. Paul Island

We extend the above approach into the local domain around St. Paul Island by applying a high-resolution numerical grid. The model data will be compared to current meter data. Eight current meters were deployed in the vicinity of St. Paul Island (Figure 9) from September 13, 1995 to August 7, 1996. All current meters were Aanderra model RCM 7. Current speed and

direction, temperature, and conductivity were sampled at hourly intervals. The compass in the instrument at mooring site 6 failed, resulting in no current data. At mooring site 1, two current meters were deployed at 25 m and 55 m in a water depth of 65 m. All other current meters were deployed close to 25 m isobath. Current records were separated into tidal (diurnal and semidiurnal periods) and subtidal oscillations. Moreover, in the fine-grid domain the two sea level measurements are available for comparison with the model results as well [Mofjeld *et al.*, 1984]. The fine-grid model (617 m resolution) has been run around St. Paul Island (see Figure 4) to provide model simulations for comparison with observations. Four major constituents are considered (M_2 , N_2 , K_1 and O_1).

Table 1 depicts a comparison between measured and computed sea level, and Table 2 shows comparison of the computed and measured cur-

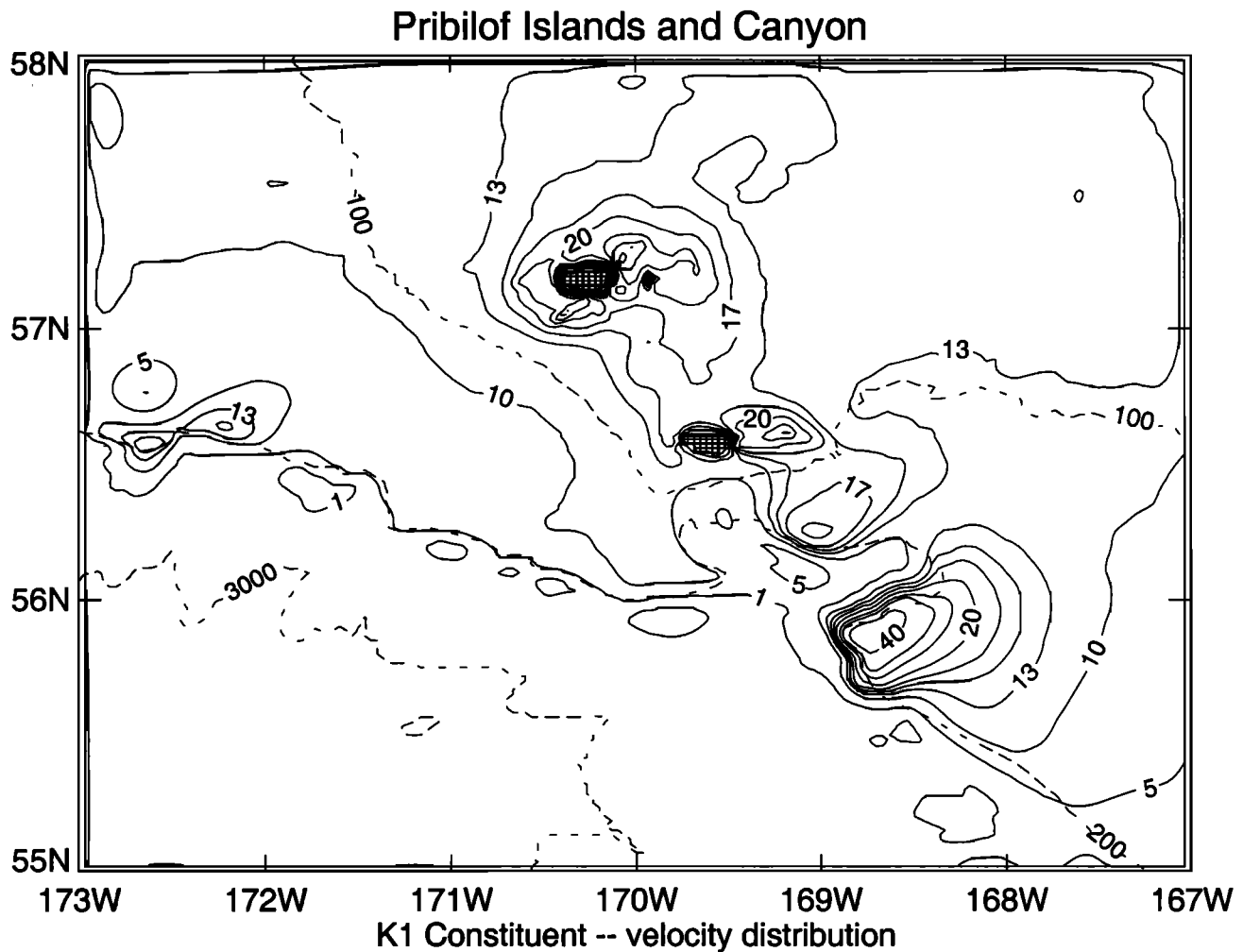


Figure 8. Contours of the maximum tidal currents (cm s^{-1}) of the K_1 wave in the Pribilof Island and Canyon domain. Dashed lines denote depth in meters.

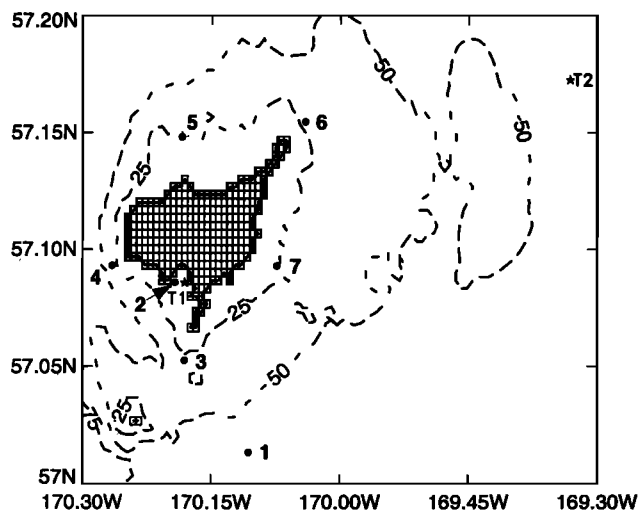


Figure 9. St. Paul mooring sites. The current meter mooring sites are indicated by circles with their appropriate number. The location of tide gages is indicated by stars.

rents. The computed and observed elevations and phases given in Table 1 are in excellent agreement. Tidal phase in this table is referred to Greenwich and is expressed in degrees. As one can glean from Table 1, the amplitude of the M_2 , the dominant constituent in the semidiurnal band, is quite close to the amplitude of the K_1 , the dominant constituent in the diurnal band.

The computed and observed currents are given in Table 2 through the various ellipse parameters. In order to compare these data the standard deviations between observed and computed values for the major axis of tidal ellipse are computed. For the M_2 and K_1 tides the standard deviation of the major axis magnitude is $\pm 1.81 \text{ cm s}^{-1}$ (average magnitude is 41.9 cm s^{-1}) and $\pm 1.47 \text{ cm s}^{-1}$ (average magnitude is 11.88 cm s^{-1}), respectively. Standard deviations for direction is 6.65° for M_2 tide and 14.1° for K_1 tide.

Table 1. Comparison of Computed and Observed Tidal Waves

Longitude	Latitude	Constituent	Amplitude H , cm		Phase G , deg	
			Observed	Computed	Observed	Computed
057°08'N	170°18'W	M_2	25.6	26.1	102.6	104.8
057°08'N	170°18'W	N_2	08.8	08.6	057.6	057.6
057°08'N	170°18'W	K_1	28.6	27.7	328.2	333.0
057°08'N	170°18'W	O_1	19.6	19.1	315.3	315.4
057°17'N	169°33'W	M_2	24.9	27.5	131.0	128.2
057°17'N	169°33'W	N_2	08.7	08.8	077.0	087.4
057°17'N	169°33'W	K_1	24.9	25.7	333.0	335.6
057°17'N	169°33'W	O_1	17.3	17.3	319.0	317.4

Phase G is referred to Greenwich.

Thus the comparison is quite satisfactory, although calculated diurnal values are often larger than the observed currents. It is difficult to explain this systematic error, but it is likely a result of the differences between the vertically averaged model and depth-dependent observations. Instruments at sites 2–7 were located about 5 m above the bottom, therefore close to the bottom boundary layer. As *Mofjeld et al.* [1984] pointed out, the thickness of the bottom boundary layer for the M_2 constituent is different from the K_1 constituent at the mid-shelf stations in the Bering Sea. Therefore the systematic error may be related to the different behavior of diurnal and semidiurnal tides near the seafloor.

The general pattern of the tidal motion deduced from Table 2 reveals that the largest tidal currents (above 70 cm^{-1}) occurred at the southern tip of St. Paul Island, close to site 3 (Figure 9). The model shows that the currents of the same magnitude occur in the vicinity of site 6 (where current meter failed). Thus the major current amplification domains are off southern and northeastern peninsulas in the shallow water domains. The directions of the major axes of the tidal ellipses given in Table 2 tend to follow the contours of constant depth.

It is evident from Table 2 that M_2 constituent dominates the tidal velocity in the vicinity of the island. An explanation of this phenomenon is related to the sea level distribution around St. Paul Island. Although, the sea level for both M_2 and K_1 is of the same order, the sea level gradients are much stronger for the M_2 constituent. The dipole structure in the sea level distribution depicted in Figures 5 and 7 drives tidal currents in the island proximity. This sea level pattern is much stronger for the M_2 tide with approximately 15 cm sea level change around St. Paul Island, as compared to about 5 cm difference for the K_1 tide. The strength of the dipole is

revealed through the phase change around St. Paul Island as well. The change of phase of the M_2 tide is approximately 15° , while the phase of K_1 is changing only 4° – 5° . Similar relations can be deduced around St. George Island, where both amplitude and phase differences are much smaller.

The dynamics of the semidiurnal or diurnal wave around islands, as gleaned from the charts given in Figures 5 and 7, seems to be quite complicated. Distribution patterns show that the maximum and minimum amplitudes are located on the opposite sides of the islands. These charts were constructed for the time when the sea level maximum occurred in the domain, and therefore the dipole position is associated with this time. At some distance from the islands the influence of a dipole structure is small, and the amplitude of the M_2 wave is approximately 30 cm. Investigation of the temporal change in the M_2 wave pattern around St. Paul Island reveals that the M_2 wave is a superposition of two waves: the primary wave of 30 cm amplitude, which propagates from the basin onto the shelf, and a secondary wave trapped around St. Paul Island. In Figure 10 the M_2 sea level is given for the four phases of the tidal wave. These phases have been chosen in proximity of the minimum, maximum, and zero sea level for the primary wave. While the primary wave changes sea level in the entire domain from approximately -30 cm to $+30 \text{ cm}$, the secondary wave of dipole structure ($\sim 7 \text{ cm}$ amplitude) propagates clockwise around St. Paul Island with the same period as the primary wave. To follow the clockwise movement of a dipole, it is sufficient to locate the maximum (or minimum) amplitude for the four phases of tidal wave in Figure 10.

6. Residual Motion Induced by Tides

To define a slowly changing subtidal motion, a low-pass filter (half-amplitude 35 hours) was

Table 2. Comparison Between Observed/Computed Ellipsis Parameters

Station	Latitude, Longitude	T. Depth, Depth	Constituent	Major, cm/s	Minor, cm/s	Direction, deg	Phase, deg
1	057°01.11'N 170°08.71'W	65 55	M_2	28.6 23.5	13.6 10.4	067 067	119 152
1	057°01.11'N 170°08.71'W	65 55	N_2	10.1 06.1	04.2 02.5	067 062	065 051
1	057°01.11'N 170°08.71'W	65 55	K_1	12.0 16.2	03.8 04.9	-100 -105	127 128
1	057°01.11'N 170°08.71'W	65 25	O_1	08.3 11.6	02.6 03.7	-100 -102	110 080
2	057°08.12'N 170°19.80'W	21 16	M_2	17.1 17.8	02.6 3.9	118 110	083 082
2	057°08.12'N 170°19.80'W	21 16	N_2	05.9 06.7	01.5 00.8	-55 -65	160 138
2	057°08.12'N 170°19.80'W	21 16	K_1	06.4 08.6	02.9 00.5	0-8 -61	056 087
2	057°08.12'N 170°19.80'W	21 16	O_1	05.8 06.8	02.7 00.4	060 -59	108 114
3	057°05.36'N 170°17.49'W	26 21	M_2	71.6 64.9	15.8 08.4	074 088	108 086
3	057°05.36'N 170°17.49'W	26 21	N_2	21.3 15.0	5.3 03.1	075 083	046 061
3	057°05.36'N 170°17.49'W	26 21	K_1	19.8 23.1	04.6 03.7	-89 -93	090 110
3	057°05.36'N 170°17.49'W	26 21	O_1	11.7 15.8	02.1 02.6	-70 -105	066 057
4	057°09.06'N 170°25.88'W	24 19	M_2	49.8 50.1	10.9 5.7	-48 -13	349 324
4	057°09.06'N 170°25.88'W	24 19	N_2	15.0 14.6	03.8 01.3	130 115	107 120
4	057°09.06'N 170°25.88'W	24 19	K_1	12.0 14.6	04.0 02.6	-44 -27	132 169
4	057°09.06'N 170°25.88'W	24 19	O_1	05.5 09.0	01.5 01.6	-25 -35	124 123
5	057°14.52'N 170°17.86'W	26 21	M_2	39.4 43.8	04.9 05.9	090 087	074 067
5	057°14.52'N 170°17.86'W	26 21	N_2	10.6 11.3	01.3 01.2	077 087	022 009
5	057°14.52'N 170°17.86'W	26 21	K_1	09.7 13.2	00.4 00.7	-85 -87	038 044
5	057°14.52'N 170°17.86'W	26 21	O_1	06.8 09.9	00.4 00.7	-86 -87	006 004
7	057°09.22'N 170°06.76'W	26 21	M_2	45.1 50.4	12.0 11.1	030 040	061 101
7	057°09.22'N 170°06.76'W	26 21	N_2	13.4 13.4	03.7 3.3	034 039	002 353
7	057°09.22'N 170°06.76'W	26 21	K_1	11.4 16.4	01.7 01.8	-15 041	171 133
7	057°09.22'N 170°06.76'W	26 21	O_1	07.3 10.2	00.6 01.0	047 044	200 170

Each station includes two lines: top line describes observed data and bottom line describes computed data. T. depth defines total depth in meters. Depth defines current meter level. Direction defines orientation of the major axis in relation to true north. The direction changes from 0° to ±180°.

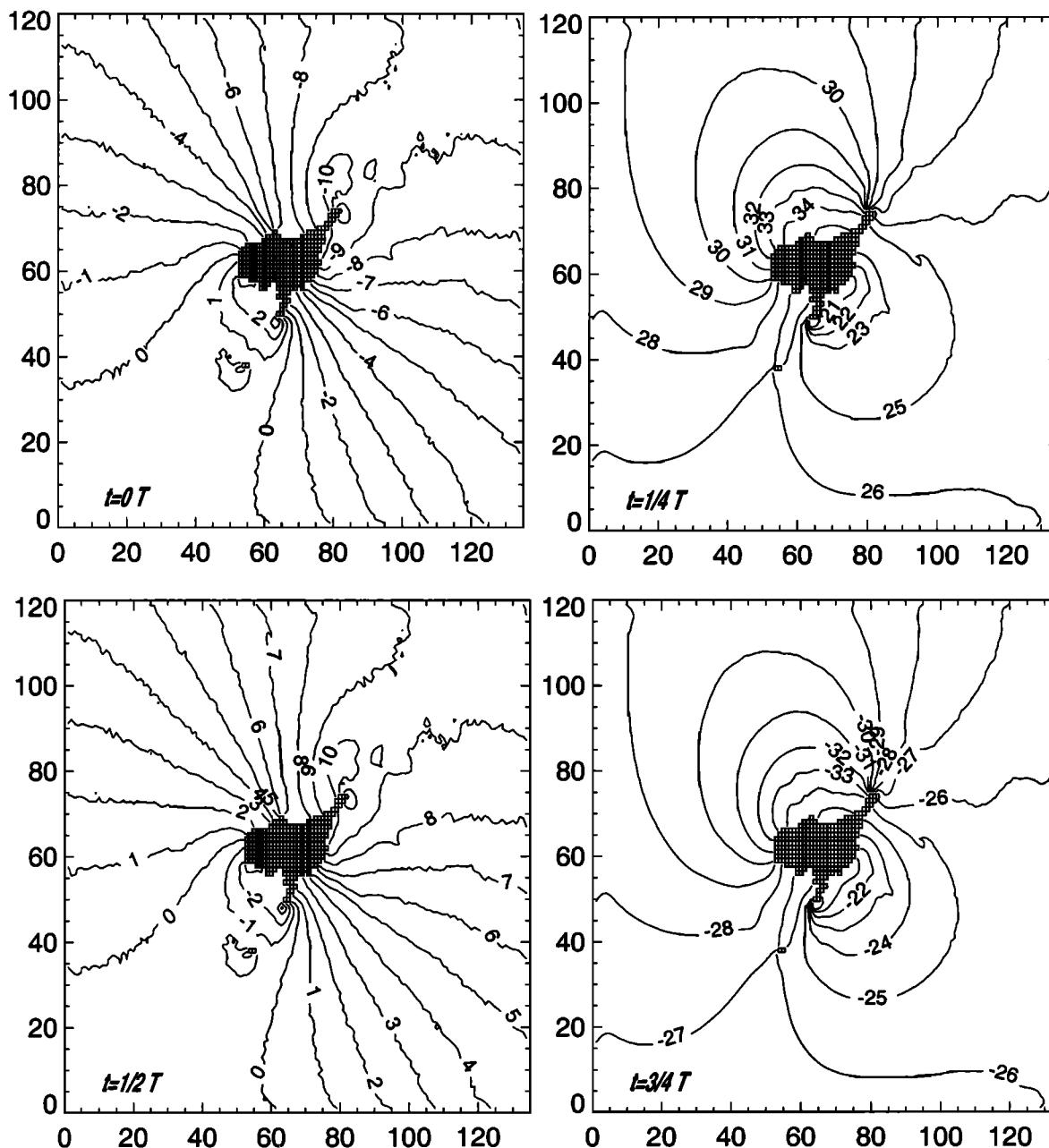


Figure 10. Sea level of the M_2 tide around St. Paul Island at the four phases of the 12.42 hour cycle.

applied to the current records obtained around St. Paul Island. Data were then resampled at 6 hour intervals (Figure 11). This filter removes the diurnal and semidiurnal tidal signal from the record. The low-frequency currents are directed along bathymetry and support clockwise circulation around the island as observed in drifter trajectories. The flow around the island for the whole measuring period depicts amazing stability in direction, only once (February 10) the flow reversal occurred. Currents around the island can be forced by density gradients or

wind; but neither of these mechanisms would result in the described stable behavior through the various seasons (Figure 11). The only constant mechanism is rectifying tidal currents into low-frequency currents. The high-resolution model constructed around St. Paul Island is used to study a permanent circulation induced through the nonlinear interactions. Residual velocities and sea level can be obtained by averaging an hourly time series over a period of 29 days. It is evident from numerical experiments performed in the entire Bering Sea and in the Pribilof Is-

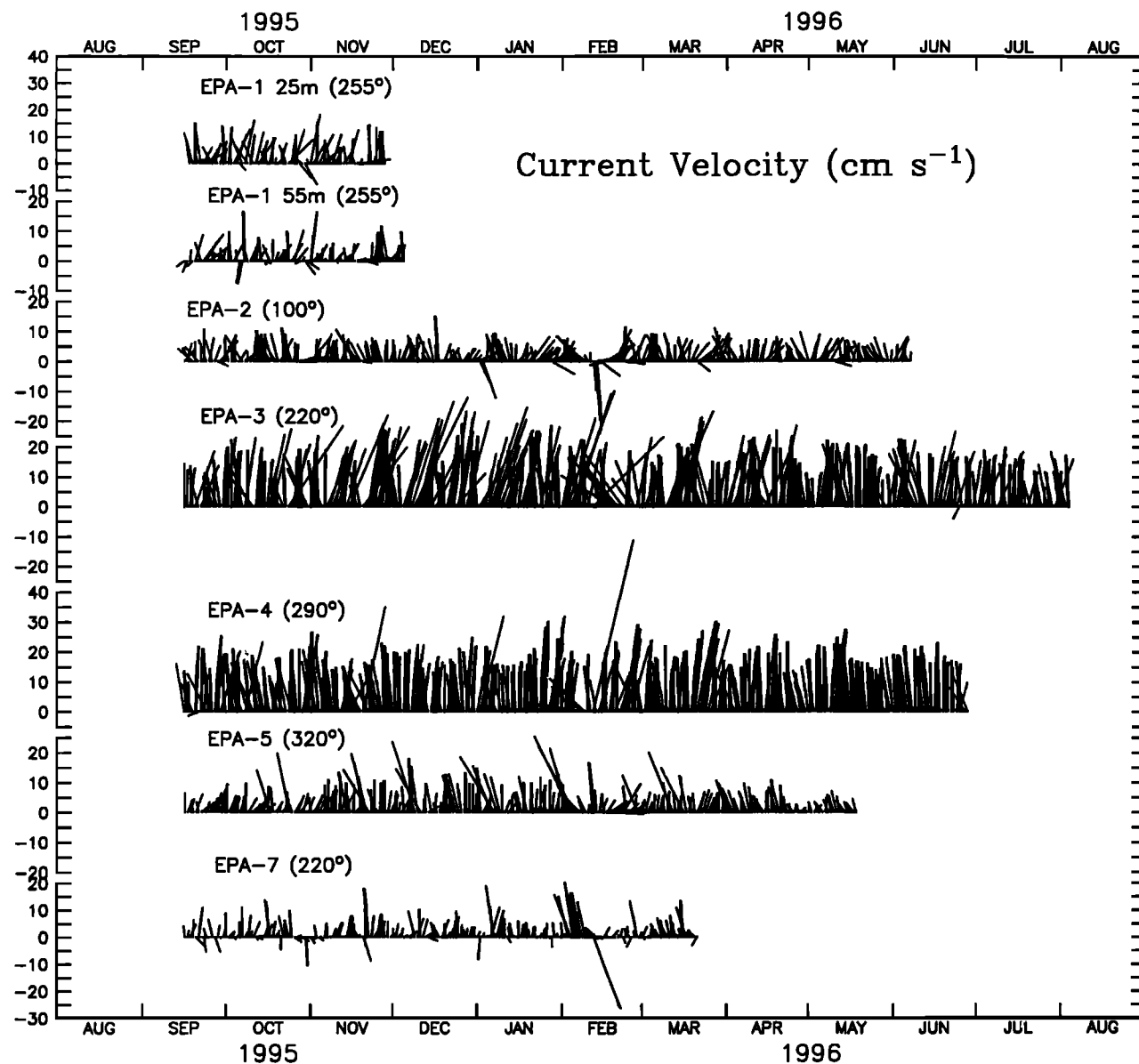


Figure 11. Time series of low-pass-filtered current data. (Resolved along net current direction.)

lands subdomain that residual currents strongly depend on the horizontal resolution of a numerical grid. Residual tidal motion calculated from a 9.26 km grid model for the whole Bering Sea reveals in the shallow areas around Pribilof Islands a velocity of 1–2 cm s^{-1} [Kowalik, 1999]. This small velocity exactly delineates the permanent clockwise rotation around the islands. The mean currents depict about a 2.5-fold increase when numerical lattice was diminished from 9.26 km to 1.852 km.

The horizontal resolution was further increased around St. Paul Island to 617 m. This resolution is close to the grid distance recommended by Zimmerman [1978] and used by Abra-

ham *et al.* [1987] for reproduction of the bottom topography with a significant production of vorticity. Calculations with this fine grid in the St. Paul subdomain confirm general clockwise circulation, and the average and maximum residual velocities have grown considerably, as can be seen in Figure 12. Maximum residual velocities have changed from approximately 10 cm s^{-1} in 1.852 km grid up to 30 cm s^{-1} in a 617 m grid. In the island vicinity the residual circulation is small and tends to be organized in local coastal eddies. At a distance of about 1 to 3 km from St. Paul Island the residual velocity attains greatest values and circles the island in a continuous fashion. The average residual currents in this re-

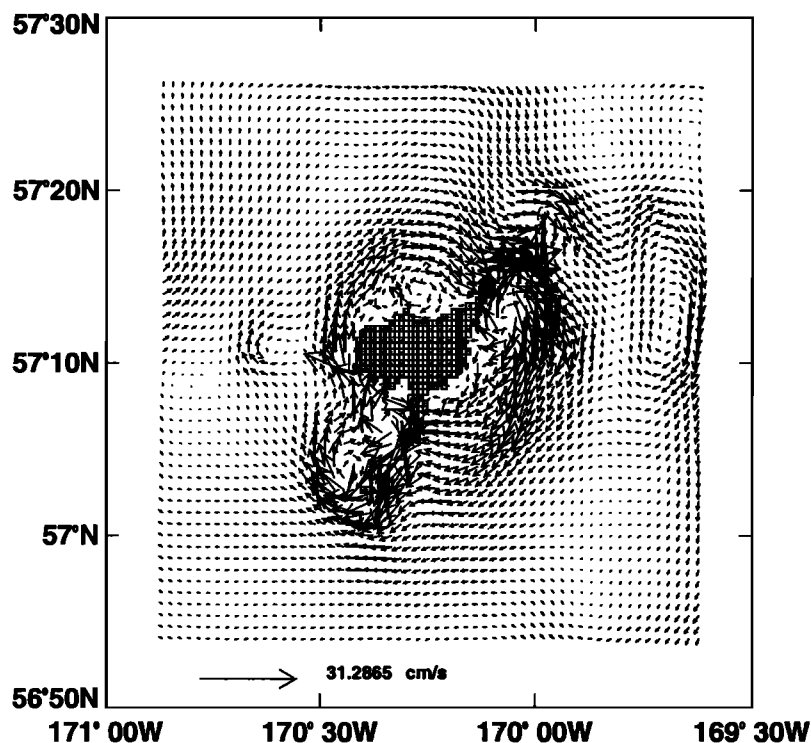


Figure 12. Residual tidal currents around St. Paul Island. Four major constituents are considered; numerical space step is 617 m.

gion are of the order of 10 to 15 cm s^{-1} , a considerable increase when compared with 1 - 2 cm s^{-1} obtained in the 9.26 km grid. Additional results obtained for the M_2 constituent computed alone, without interaction with the remaining tidal constituents, show that this constituent is primarily responsible for the generation of residual currents around St. Paul Island.

A comparison of the measured residual currents with the currents obtained from the above computation is given in the Figure 13. Computed current magnitude and direction turned out to be in good agreement with the current obtained from the observations. The most interesting is the current pattern at sites 2 and 5. There, because of the local interaction with the bottom slope and coastline, the measured currents have been deflected from the general clockwise circulation. The local coastal eddies, evident in the fine-resolution model (Figure 12), are responsible for this deflected flow pattern.

7. Particle Motion Induced by Tides

The trajectories of satellite-tracked drifters depict a well-developed clockwise flow around the Pribilof Islands. Although residual clockwise motion (Figures 11, 12, and 13) would result in the clockwise rotation, the oscillating

tidal motion is important as well, because it causes excursions of the water particle of the order of 3 to 12 km (the approximate diameter of St. Paul and St. George Islands). It is obvious from our observations that the general pattern of circulation plays an important role in

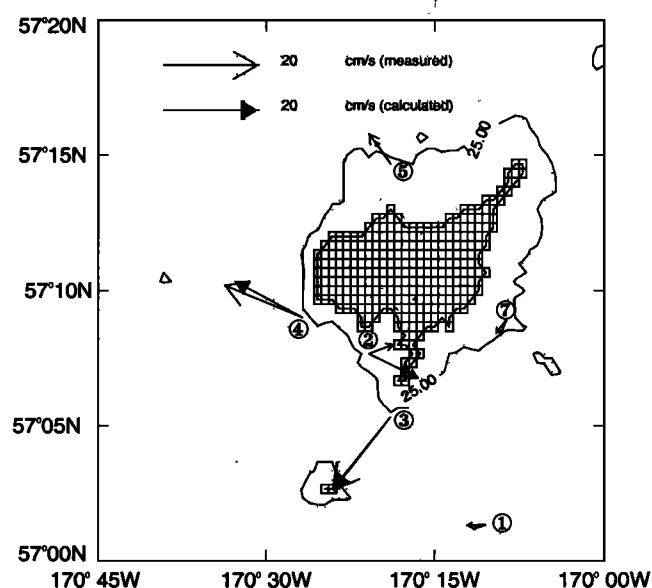


Figure 13. Residual currents in the vicinity of St. Paul Island: measured, open arrowheads; calculated, solid arrowheads.

generating trajectories trapped around islands, diverting the buoys into and out of close proximity of the islands.

To depict a pattern of the tidal motion in the island's proximity, a set of particles is released around St. Paul. The position of a water particle located at a point with coordinates (x_0, y_0) at time $t = t_0$ is tracked in time via the Lagrangian velocity. The Lagrangian velocity is defined as superposition of Eulerian velocity (i.e., velocity given from tidal computation) and Stokes velocity. The change in position of a specific particle in the horizontal plane during time step dt is described as the total effect due to Eulerian and Stokes velocities [Longuet-Higgins, 1969]:

$$dx = udt + 0.5\left(u\frac{\partial u}{\partial x} + v\frac{\partial u}{\partial y}\right)(dt)^2, \quad (11a)$$

$$dy = vdt + 0.5\left(u\frac{\partial v}{\partial x} + v\frac{\partial v}{\partial y}\right)(dt)^2. \quad (11b)$$

From the experiments carried out we can conclude that the primary factors are Eulerian oscillatory and residual velocity. The Stokes velocity is of secondary importance in the particle motion around St. Paul Island.

To depict trajectories in the St. Paul Island region, a number of particles are released to the west from the island. The initial locations and trajectories of the particles are given in Figure 14. Out of five particles released, the one initially located 1 km from the shore describes the fastest trajectory. The particle released closest to the island is slowed down by the local coastal eddies. Only particles within 6 km of the island describe major features of the clockwise trapped motion. Particles initially located greater than 8 km west of the island were trapped into local offshore eddy generated around shallow bank (see Figure 12).

We do not have a large enough set of measurements of buoy trajectories around the islands to perform statistical analysis and comparison against model computations. It is interesting to notice that trajectory of the fastest particle in Figure 14 (St. Paul Island region) and satellite-tracked buoy trajectory in Figure 3 (St. George Island region) show a markedly similar period of rotation (~ 6 days) and pattern of the very small tidal ellipses.

8. Discussion

Satellite-tracked buoys deployed in 1993 and in 1995 depicted circulation at the shelf break with tidal loops. In the region of Pribilof Islands the buoys were trapped in clockwise cir-

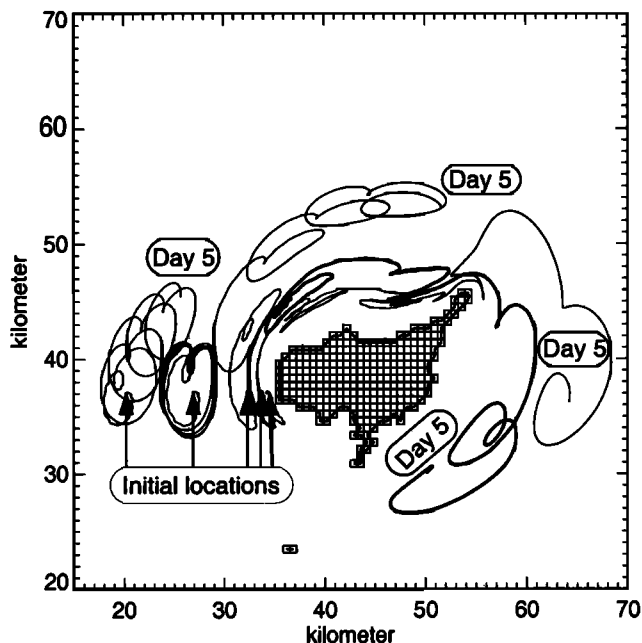


Figure 14. Calculated trajectories during 5 day period. Particles are released west of St. Paul Island. Lagrangian particle motion is a superposition of tidal motion (oscillatory and residual) and Stokes drift. Mean velocity varies from 10 to 15 cm s^{-1} .

ulation. The long series of current meter data obtained in 1995 and 1996 around St. Paul Island were filtered into tidal and subtidal oscillations. These data demonstrate a dominance of the tidal motion in the flow pattern around the island. Measurements depicted the M_2 tidal current up to 70 cm s^{-1} . The model investigations show that tidal motion around the island is driven by dipole structure of the sea level oscillations. The temporal pattern of the M_2 tide around St. Paul Island elucidates that this wave is a superposition of two waves: the main wave, which propagates from the Pacific, and the secondary wave of dipole structure trapped around the island. The dipole is much stronger for the semidiurnal oscillations. The observed residual clockwise flow is very steady in direction with only a few reversals during the observational period. The observational results are consistent with tidal model simulations both for the oscillatory and for the residual motion. The residual flow pattern as revealed by the model is a clockwise flow through with quite a few small coastal eddies that locally reverse flow direction due to topographic steering. The source of this trapped motion are nonlinear interactions of strong tidal motion with the island topography.

A series of numerical experiments was carried out to investigate the dependence of residual flow on the horizontal resolution of the model.

A two-dimensional model of 9.26 km resolution gives an average velocity of about 1-2 cm s⁻¹. At a resolution of 1.852 km the average current is about 3-5 cm s⁻¹. A resolution of 617 m increases average flow to 10-15 cm s⁻¹. Zimmerman [1978] and Robinson [1981] suggested that the tidal excursion length ought to be resolved by the numerical grid for proper resolution of the nonlinear terms and vorticity, which is generated over bottom topography. At a resolution of 617 m around St. Paul Island the tidal excursions of the water particle are of the order of 3 to 12 km; therefore it seems that recommendations put forward by Zimmerman [1978] and Robinson [1981] are fulfilled in this high-resolution grid for proper simulation of the residual motion.

Enhanced tidal current causes enhanced vertical mixing erasing stratification and building a local tidal front in proximity to the Pribilof Islands. Both islands are surrounded by structure fronts [Schumacher and Stabeno, 1998] which divide the well-mixed inner shelf waters (0-40 m) from the two layer structure characteristic of the middle shelf (50-100 m). Such a density structure at the middle shelf may also, by geostrophy, generate currents directed around the islands. Thus tidally generated residual motion in the island proximity may be superseded by the density-driven motion at larger distances from the islands.

Our observations and computations of enhancement of the tidal currents around Pribilof Islands are confirmed by larger-scale observations of Mofjeld [1986] and modeling of Liu and Leendertse [1990] and Kowalik [1999]. Enhanced currents result in the mean residual flow, which can be a major driving mechanism for circulation around islands and in the passages between the Aleutian Islands and possibly for exchange between basin and shelf. The homogenization of water properties around Pribilof Islands, in Aleutian Island Passes [Reed et al., 1993; Reed and Stabeno, 1994] through the tidal motion, and relatively strong residual tidal baroclinic flow demonstrated by Liu and Leendertse [1990] should have a bearing on how tidal effects are to be incorporated into mechanisms that contribute to the exchange of properties between the North Pacific and the Bering Sea, between islands and surrounding shelf and between deep basin and shelf.

Acknowledgments. We are indebted to anonymous referees for their comments and improvements that strengthened the paper. Z. Kowalik gratefully acknowledges support for this work from the Office of Naval Research under grant N00014-95-1-0929 and from Cooperative Institute for Arctic Research, University of Alaska.

References

- Abraham, G., H. Gerritsen, and G. J. H. Lindijer, Subgrid tidally induced residual circulation, *Cont. Shelf Res.*, 7, 285-305, 1987.
- Brink, K. H., Tidal and lower frequency currents above Fieberling Guyot, *J. Geophys. Res.*, 100, 10 817-10 832, 1995.
- Coachman, L. K., Circulation, water masses, and fluxes on the southeastern Bering Sea shelf, *Cont. Shelf Res.*, 5, 23-108, 1986.
- Defant, A., *Physical Oceanography*, vol. 2, 598 pp. Pergamon, New York, 1960.
- Gill, A. E., *Atmosphere-Ocean Dynamics*, 662 pp. Academic, San Diego, Calif., 1982.
- Gjevik, B., and M. Moe, Steady and transient flow around banks located near a shelf edge, *Cont. Shelf Res.*, 14, 1389-1409, 1994.
- Haidvogel, D. B., A. Beckmann, D. C. Chapman, and R.-Q. Lin, Numerical simulation of flow around a toll isolated seamount. Part II: Resonant generation of trapped waves, *J. Phys. Oceanogr.*, 23, 2373-2391, 1993.
- Hendershott, M. C., Numerical models of ocean tides, in *The Sea*, vol. 6, pp. 47-96, John Wiley, New York, 1977.
- Johnson, W. R., and Z. Kowalik, Modeling of storm surges in the Bering Sea and Norton Sound, *J. Geophys. Res.*, 91, 5119-5127, 1986.
- Klinck, J. M., Circulation near submarine canyons: A modeling study, *J. Geophys. Res.*, 101, 1211-1223, 1996.
- Kowalik, Z., Bering Sea tides. In: *The Bering Sea: Physical, Chemical and Biological Dynamics*, edited by T. R. Loughlin and K. Ohtani, Alaska Sea Grant Press, Fairbanks, AK, pp. 93-127, 1999.
- Kowalik, Z., and A. Y. Proshutinsky, Topographic enhancement of tidal motion in the western Barents Sea, *J. Geophys. Res.*, 100, 2613-2637, 1995.
- Liu, S. K., and J. J. Leendertse, Modeling of the Alaskan continental shelf waters, *OCSEAP Final Rep*, 70, pp. 123-275, NOAA, Anchorage, Alaska, 1990.
- Loder, J.W., Topographic rectification of tidal currents on the sides of Georges Bank, *J. Phys. Oceanogr.*, 10, 1399-1416, 1980.
- Longuet-Higgins, M. S., On the transport of mass by the time-varying ocean currents, *Deep Sea Res.*, 16, 431-447, 1969.
- Mofjeld, H. O., Observed tides on the Northeastern Bering Sea shelf, *J. Geophys. Res.*, 91, 2593-2606, 1986.
- Mofjeld, H. O., J. D. Schumacher and D. J. Pashinski,

- Theoretical and observed profiles of tidal currents at two sites of the southeastern Bering Sea shelf, NOAA Tech. Memo. ERL PMEL-62. 60pp., Seattle, Washington, 1984.
- Pearson, C. A., H. O. Mofield, and R. B. Tripp, Tides of the eastern Bering Sea shelf, in *The Eastern Bering Sea Shelf: Oceanography and Resources*, edited by D. W. Hood, and J. A. Calder, pp. 111-130, Natl. Oceanic and Atmos. Admin., Juneau, Alaska, 1981.
- Pingree, R. D., and L. Maddock, Rotary currents and residual circulation around banks and islands, *Deep Sea Res., Part A*, 32, 929-947, 1985.
- Reed, R.K., and P.J. Stabeno, Flow along and across the Aleutian Ridge, *J. Mar. Res.*, 52, 639-648, 1994.
- Reed, R.K., and P.J. Stabeno, On the climatological mean circulation over the eastern Bering Sea shelf, *Cont. Shelf Res.*, 16, 1297-1305, 1996.
- Reed, R.K., G.V. Khen, P.J. Stabeno, and A.V. Verkhunov, Water properties and flow over the deep Bering Sea basin, summer 1991, *Deep Sea Res.*, 40(11/12), 2325-2334, 1993.
- Robinson, I. S., Tidal vorticity and residual circulation, *Deep Sea Res., Part A*, 28, 195-212, 1981.
- Schumacher, J. D., and T. H. Kinder, Low-frequency current regimes over the Bering Sea shelf, *J. Phys. Oceanogr.*, 13, 607-623, 1983.
- Schumacher, J.D., and R. K. Reed, Characteristics of currents over the continental slope of the Bering Sea, *J. Geophys. Res.*, 97, 9423-9433, 1992.
- Schumacher, J.D., and P.J. Stabeno, The continental shelf of the Bering Sea, *The Sea*, edited by A. Robinson and K. Brink, vol., 11, pp. 789-821, John Wiley, New York, 1998.
- Zimmerman, J. T. F., Topographic generation of residual circulation by oscillatory (tidal) currents, *Geophys. Astrophys. Fluid Dyn.*, 11, 35-47, 1978.

Z. Kowalik, Institute of Marine Science, University of Alaska, Fairbanks, AK 99775. (ffzk@ims.uaf.edu)

P. Stabeno, PMEL/NOAA, 7600 Sand Point Way, Seattle, WA 98115. (stabeno@pmel.noaa.gov)

(Received July 21, 1998; revised June 6, 1999; accepted July 7, 1999.)